

## Metamorphosis of discontinuity lines and rectification of magnetic flux avalanches in the presence of noncentrosymmetric pinning forces

M. Motta<sup>1</sup>, L. Burger<sup>2</sup>, Lu Jiang<sup>3</sup>, J. D. González Acosta<sup>4,5</sup>, Ž. L. Jelić<sup>6,5,6</sup>, F. Colauto<sup>1</sup>, W. A. Ortiz<sup>1</sup>,  
T. H. Johansen<sup>7</sup>, M. V. Milošević<sup>8</sup>, C. Cirillo<sup>8</sup>, C. Attanasio<sup>8,9</sup>, Cun Xue<sup>10</sup>,  
A. V. Silhanek<sup>11</sup> and B. Vanderheyden<sup>2,\*</sup>

<sup>1</sup>*Departamento de Física, Universidade Federal de São Carlos, 13565-905 São Carlos, São Paulo, Brazil*

<sup>2</sup>*Montefiore Research Unit, Department of Electrical Engineering and Computer Science, Université de Liège, 4000 Sart Tilman, Belgium*

<sup>3</sup>*School of Aeronautics, Northwestern Polytechnical University, Xi'an 710072, China*

<sup>4</sup>*Facultad de Ingeniería, Universidad del Magdalena, Santa Marta, Colombia*

<sup>5</sup>*Departement Fysica, Universiteit Antwerpen, Groenenborgerlaan 171, B-2020 Antwerpen, Belgium*

<sup>6</sup>*Nokia Bell Labs, Antwerp, Belgium*

<sup>7</sup>*Department of Physics, University of Oslo, POB 1048, Blindern, 0316 Oslo, Norway*

<sup>8</sup>*CNR-SPIN, c/o Università degli Studi di Salerno, I-84084 Fisciano (Sa), Italy*

<sup>9</sup>*Dipartimento di Fisica "E.R. Caianiello", Università degli Studi di Salerno, I-84084 Fisciano (Sa), Italy*

<sup>10</sup>*School of Mechanics, Civil Engineering and Architecture, and MIIT Key Laboratory of Dynamics and Control of Complex Systems, Northwestern Polytechnical University, Xi'an 710072, China*

<sup>11</sup>*Experimental Physics of Nanostructured Materials, Q-MAT, CESAM, Université de Liège, B-4000 Sart Tilman, Belgium*



(Received 17 March 2021; revised 19 May 2021; accepted 19 May 2021; published 9 June 2021)

Considering a noncentrosymmetric pinning texture composed of a square array of triangular holes, the magnetic flux penetration and expulsion are investigated experimentally and theoretically. A direct visualization of the magnetic landscape obtained using a magneto-optical technique on a Nb film is complemented by a multiscale numerical modeling. This combined approach allows the magnetic flux dynamics to be identified from the single flux quantum limit up to the macroscopic electromagnetism response. Within the theoretical framework provided by time-dependent Ginzburg-Landau simulations, an estimation of the in-plane current anisotropy is obtained and its dependence with the radius of the curvature of hole vertices is addressed. These simulations show that current crowding plays an important role in channeling the flux motion, favoring hole-to-hole flux hopping rather than promoting interstitial flux displacement in between the holes. The resulting anisotropy of the critical current density gives rise to a distinct pattern of discontinuity lines for increasing and decreasing applied magnetic fields, in sharp contrast to the invariable patterns reported for centrosymmetric pinning potentials. This observation is partially accounted for by the rectification effect, as demonstrated by finite-element modeling. At low temperatures, where magnetic field penetration is dominated by thermomagnetic instabilities, highly directional magnetic flux avalanches with a fingerlike shape are observed to propagate along the easy axis of the pinning potential. This morphology is reproduced by numerical simulations. Our findings demonstrate that anisotropic pinning landscapes and, in particular, ratchet potentials produce subtle modifications to the critical state field profile that are reflected in the distribution of discontinuity lines.

DOI: [10.1103/PhysRevB.103.224514](https://doi.org/10.1103/PhysRevB.103.224514)

### I. INTRODUCTION

The physics of mechanical ratchet and pawl systems were popularized by Feynman's lectures [1] as an ingenious mechanism seemingly defying the second law of thermodynamics by extracting work from a system in thermal equilibrium. Feynman and many authors afterwards elucidated the thermodynamic physics involved in this process by showing that the system must be out of equilibrium for the ratchet effect to be operative [2]. Later on, general conditions and the associated set of rules for achieving a net displacement of particles with zero-mean excitations were clearly established [3]. Nowadays, it is widely recognized that the physics of

ratchet systems is at the root of many different applications, such as molecular motors in the biological realm [4], particle separation [5], directional cell migration [6,7], rectification of self-propelled swimmers [8–11], and Leidenfrost-based liquid pumping [12,13].

Particular interest has been devoted to the ratchet of magnetic flux quanta in superconductors [14,15] due to the unmatched versatility of these systems to readily and independently adjust the density of particles and the strength of the interacting potential. Besides being a playground of choice for investigating the vortex ratchet, asymmetric ratchet potentials have been proposed as a practical approach to remove unwanted flux from certain sensitive areas in devices such as superconducting quantum interference device (SQUID) detectors [14]. Although the directional flux motion induced by ratchets is by now very well understood at the microscale

\*B.Vanderheyden@uliege.be

[16,17], little is known about the impact of noncentrosymmetric pinning landscapes on the magnetic flux distribution at the macroscale.

In 2007, Albrecht *et al.* [18] investigated the penetration of magnetic flux in a 200-nm-thick  $\text{MgB}_2$  film with an asymmetric pinning landscape produced by substrate surface steps of one unit cell. In the smooth magnetic flux penetration regime taking place at the highest investigated temperatures, the critical current densities were determined from the distribution of magnetic flux density in the remanent state. The very weak unidimensional vertical modulation ( $\sim 0.38$  nm) was shown to yield an anisotropy of only a few percent between the critical current densities flowing, respectively, along and perpendicular to the steps. In contrast, in the regime where the flux penetration was subject to thermomagnetic instabilities and for which sudden bursts of magnetic flux avalanches develop, a much stronger anisotropy was observed, with magnetic flux avalanches propagating far more easily perpendicular to the steps. However, their activity and morphology were similar irrespective of whether the propagation occurred along the easy or the hard direction of the asymmetric pinning landscape. This may not come as a surprise considering that the coherence length of  $\text{MgB}_2$  exceeded the period of the pinning lattice. Later on, Menghini *et al.* [19] investigated the magnetic flux avalanche regime in Pb films with a square lattice of asymmetric pinning potentials formed by two antidots of different sizes. In this case, since the pinning sites were substantially larger than the coherence length and the penetration depth of Pb, a very clear directional flux penetration was observed. At high temperatures, a fingerlike flux front progressed more favorably along the hard direction of the ratchet potential. At intermediate temperatures, an isotropic flux front developed, whereas at low temperatures, avalanches burst into the sample along the easy direction of the asymmetric pinning landscape. Both results, in  $\text{MgB}_2$  and in Pb, were satisfactorily explained within a thermomagnetic model for the dendritic instability described in Ref. [20]. Nevertheless, it is puzzling that no manifestation of the ratchet effect on the smooth magnetic flux penetration has been reported.

In this work, we investigate the directional magnetic flux penetration in a square array of triangular holes, a prototypical example of ratchet pinning potential. The sample is described in Sec. II and two regimes of magnetic flux penetration are studied with magneto-optical imaging technique in Sec. III. First, for the smooth penetration regime at  $T = 5$  K, it is experimentally observed that the trapped flux pattern formed during a zero-field-cooled magnetization exhibits a gradual change in shape. The central discontinuity line, separating two regions with current flowing in opposite directions, changes from a horizontal orientation to a vertical one as the external field is lowered. Second, for the thermomagnetically unstable regime at 2.5 K, it is shown that the network of triangular holes leads to magnetic flux jets with flux avalanches propagating preferentially along the easy direction. In Sec. IV, these results are analyzed by means of numerical models in a multiscale approach. First, a time-dependent Ginzburg-Landau model of a similar system with the same density of holes is used to investigate the anisotropy in the critical current densities and their dependence with the applied magnetic field. A finite-element model of the smooth penetration regime is

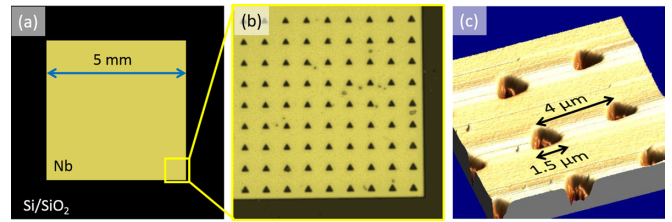


FIG. 1. (a) Schematic representation of nanostructured superconducting Nb sample (yellowish square) with a square array of triangular holes on  $\text{Si}/\text{SiO}_2$  substrate (black layer). (b) Bright field optical microscopy image of the array of holes taken at the lower-right corner of the sample. (c) Atomic force microscopy image of a  $10 \times 10 \mu\text{m}^2$  area.

then constructed that integrates the dependence of the current densities with the direction and magnetic field, but now with parameters being adapted to the experimental observations. This model is shown to reproduce the metamorphosis of the central discontinuity line (d-line). Last, a model for the flux avalanches is used to study the anisotropic penetration of such avalanches and their morphology as a function of the size and period of the array of holes. A summary of the results and conclusions are given in Sec. V.

## II. SAMPLE PREPARATION

The investigated samples were lithographically defined Nb films deposited by UHV dc magnetron sputtering with thickness of 45 nm on top of  $\text{Si}/\text{SiO}_2$  substrates. The geometrical characteristics of the patterned samples, obtained via lift-off processing, are shown in Fig. 1 and consist of a square array of period  $4 \mu\text{m}$  with equilateral triangular motifs of side  $1.5 \mu\text{m}$  covering the entire  $5 \times 5 \text{mm}^2$  Nb film. The triangular motifs are through holes, as corroborated by the atomic force microscopy images shown in Fig. 1(c). The critical temperature of the sample is  $T_c = 6.8$  K.

Using the temperature derivative of the upper critical field near  $T_c$  and the dirty limit expressions [21], we estimate the zero temperature superconducting coherence length,  $\xi(0) \sim 8$  nm, and penetration depth,  $\lambda(0) \sim 132$  nm, for the Nb film. Therefore, for the whole temperature range investigated here, the size of the triangular holes largely exceeds  $\xi$  and  $\lambda$ . The distance between the sample borders and the closest rows of triangular holes is  $1 \mu\text{m}$  all along the sample perimeter so as to avoid pronounced asymmetric edge barriers [22].

The magneto-optical (MO) technique employed for imaging the flux penetration morphology is based on the occurrence of the Faraday effect in an indicator film placed on top of the superconducting specimen [23]. The indicators used in the present work are Bi-substituted yttrium iron garnet films (Bi:YIG) with in-plane magnetization [24]. In all measurements, the magnetic field was applied perpendicular to the film plane.

## III. MAGNETO-OPTICAL INVESTIGATION

### A. Anisotropy of the critical current density

In the investigated sample, several coexisting symmetries may influence the penetration of magnetic flux. First, the

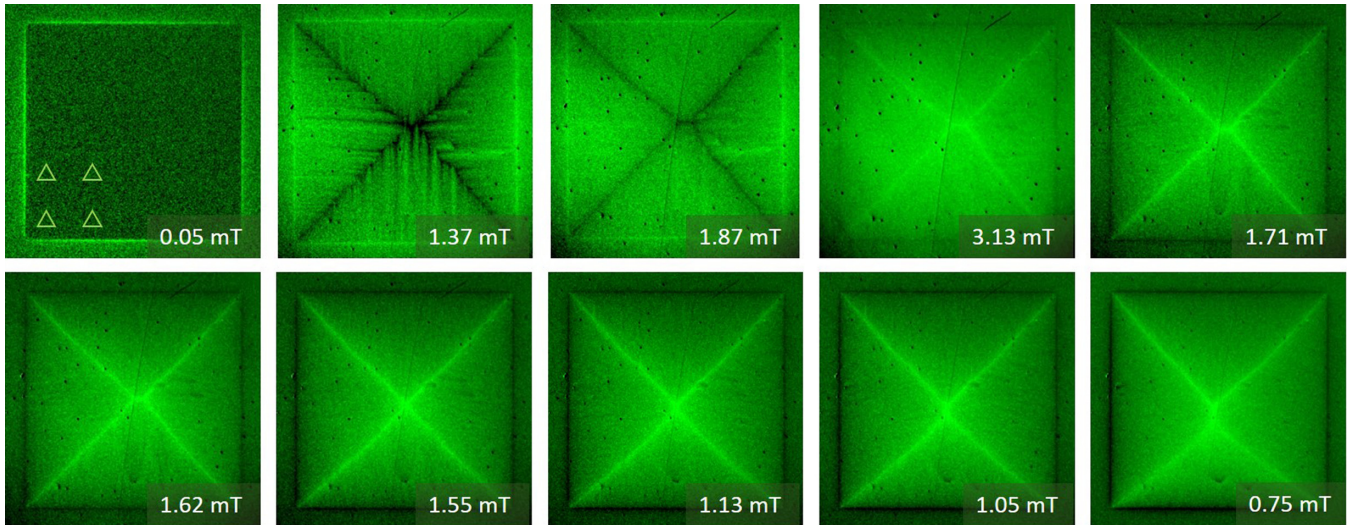


FIG. 2. Selected set of magneto-optical images at  $T = 5$  K for the square Nb sample with triangular holes oriented as shown in the first figure. Starting from the upper-left corner, the field is increased up to 8 mT and then decreased. The first three images correspond to an increasing field; the remaining ones to a decreasing field. The d-lines are seen to move laterally and vertically, while the orientation of the central d-line changes as the field is decreased.

square shape of the sample, with random pinning, imposes a critical state at full penetration with current densities flowing parallel to the sample edges. Thus, the superconducting current density is organized in sectors delimited by the so-called discontinuity lines (or d-lines), where the current density abruptly changes its direction. These lines are easy to identify by MO imaging in thin films, as they generate a sharp variation of the magnetic field component perpendicular to the film. For an isotropic sample, the expected pattern of penetrated flux has two diagonal d-lines crossing at the center of the sample. The second symmetry in the system is related to the square array of holes, which has the same  $C_4$  symmetry as the sample borders and is not expected to modify the d-line patterns. However, the placement of holes along a square array may affect the propagation of magnetic flux avalanches, as the rows and columns of the array may form preferential channels of vortex penetration [25–28]. The third symmetry is the  $C_3$  symmetry of the triangular pinning centers. A first effect comes from the fact that the triangular shape of the holes offers slightly larger cross sections for currents flowing along the  $x$  direction than for those flowing along the  $y$  direction. As a result, a slight current anisotropy breaking the  $C_4$  symmetry is expected. A second source of  $C_4$  symmetry breaking arises from the pinning landscape. As will be confirmed by the time-dependent Ginzburg-Landau analysis of Sec. IV A, the pinning force is weaker for vortices moving out in the direction of the triangle tip (moving up, along the easy axis) and stronger for vortices moving towards the triangle base (moving down, along the hard axis). This additional breaking of the  $C_4$  symmetry gives rise to a ratchet effect, with consequences on both the critical state and thermomagnetic avalanches in the system.

### B. Critical states

Figure 2 shows magneto-optical images of our sample at 5 K after zero-field cooling. At  $\mu_0 H = 0.05$  mT, the flux

is expelled from the superconducting film and accumulates at its borders. At  $\mu_0 H = 1.37$  mT, the magnetic field has nearly entirely penetrated the sample and an X-shape d-line pattern is generated, while the precursor of a central horizontal discontinuity line also appears to form. By further increasing the field to  $\mu_0 H \geq 1.8$  mT, a horizontal d-line at the center of the structure clearly develops, evidencing an asymmetry between the different sectors delimited by the d-lines. After the maximum applied field  $\mu_0 H \geq 8$  mT has been achieved, the applied field is decreased and the d-lines change from dark to bright contrast. The MO images corresponding to a field decreasing from  $\mu_0 H \geq 3.13$  mT down to  $\mu_0 H \geq 0.75$  mT unveil a progressive evolution of the central horizontal d-line towards a central vertical d-line. The fact that the d-line pattern can evolve during the decreasing magnetic field is a remarkable behavior, which has never been observed in systems with centrosymmetric pinning forces.

### C. Thermomagnetic avalanches

For  $T = 4$  K, the smooth penetration regime breaks down and the regime of abrupt magnetic flux avalanches is accessed. The MO images obtained at  $T = 2.5$  K, after zero-field cooling and progressively increasing the magnetic field, are shown in Fig. 3.

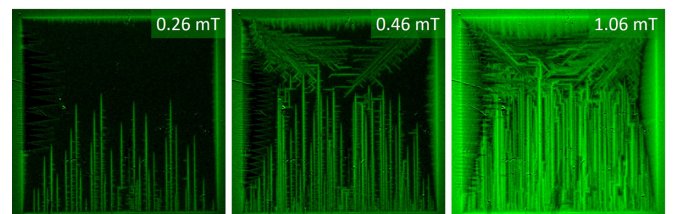


FIG. 3. Anisotropic penetration of magnetic flux avalanches of thermomagnetic origin as observed by magneto-optical imaging at 2.5 K.

At low fields, the avalanches are seen to penetrate exclusively from the bottom border and develop along an easy-axis direction with a well-defined needlelike shape and very short perpendicular branching. At high fields, avalanches are also triggered at the top edge and show 45-degree ramifications, as those observed in thin films decorated with a square array of square holes [29,30]. Moreover, 90-degree branches also develop and follow the main directions of the square lattice of holes.

In contrast to the highly anisotropic thermomagnetic avalanches reported in Ref. [18], the flux avalanches do not develop perpendicularly to the easy direction, but parallel to it.

#### IV. MULTISCALE NUMERICAL MODELS

The consequences of the symmetries of the triangular hole pinning array are investigated within a multiscale analysis. The first model, formulated with the Ginzburg-Landau equations at the scale of single vortices, allows us to estimate the variations of the critical current density as a function of the direction of flow and the geometry of the triangular holes. The second model is based on continuous electrodynamics and is used to determine the patterns of d-lines obtained in the fully penetrated state and in the remanent state for an anisotropic critical current density exhibiting a ratchet effect. The last model, also based on continuum electrodynamics, is devoted to the study of thermomagnetic avalanches in the presence of the array of triangular holes.

##### A. Time-dependent Ginzburg-Landau simulations

As a first step, we focus on the interactions between the superconducting condensate populated by the magnetic flux quanta (vortices) and the asymmetric pinning potential. The time-dependent Ginzburg-Landau (TDGL) framework is selected for this task as it can describe the complex interplay among the vortices in arbitrary geometries, in the presence of externally applied magnetic fields and currents, at temperatures close to the superconducting transition temperature  $T_c$ . Such an approach was recently considered for the study of a hexagonal array of triangular antidots in Al thin films [31]. Here, the TDGL numerical simulations were performed in the effective type-II limit, i.e.,  $\kappa^* = \Lambda/\xi \gg 1$ , where  $\Lambda = 2\lambda^2/d$  is the effective Pearl penetration depth,  $\lambda$  is the penetration depth,  $d$  is the thickness of the film,  $\xi$  is the coherence length, and the thin-film limit  $d \ll \lambda$  is assumed. The material and geometric properties are extracted from the experimental data. In the following section, we focus on the main results from the TDGL analysis, while we report the specifics of the numerical method in Appendix A 1.

We start our analysis by investigating the superconducting response of a specimen corresponding to an experimental unit cell of area  $L \times L$  ( $L = 8 \mu\text{m}$ ) with four equilateral triangular holes of size  $a = 1.5 \mu\text{m}$  and arranged in a square lattice of period  $W = 4 \mu\text{m}$ , as shown in the sketch in Fig. 4(a). The specimen is exposed to the perpendicular external field  $B$  and the gradually increasing in-plane injected electrical current density  $J$ , which in turn gives rise to the finite voltage in the system. From the obtained voltage-current density character-

istics  $V(J)$  [see top inset in Fig. 4(a)] and based on the point where the extracted voltage reaches the value of  $20 \mu\text{V}$ , we are able to determine the critical current density  $J_c$  at which the onset of vortex dynamics occurs (see Appendix A 1 for more details). The obtained  $J_c$  is represented as a function of the applied magnetic field as well as the direction of the applied current, which is summarized in Fig. 4. For convenience, we introduce the notation  $J_c(\theta, B)$  [or, when possible,  $J_c(\theta)$  for the sake of simplicity], where  $\theta$  indicates the angle of the direction along which the current density was applied to the system, relative to the  $x$  axis [see the bottom sketch in Fig. 4(a)]. In the absence of any additional random pinning, the critical current density exhibits a monotonic field dependence in the considered  $B$  range, as well as an anisotropic character, as seen in Fig. 4(a). More specifically, there is a ratchet asymmetry that is apparent when comparing cases where  $J$  is injected along either the positive  $x$  axis [ $J_c(0, B)$ ] or the negative  $x$  axis [ $J_c(\pi, B)$ ]. This effect is the consequence of the phenomenon of vortex rectification [32], associated with the existence of an easy (+ $y$ ) and a hard ( $-y$ ) direction for magnetic flux displacement. As a side note, the same effect can be obtained by changing the polarity of  $B$ , while keeping the direction of  $J$  fixed along the  $+x$  axis.

Besides the  $\theta = 0$  and  $\theta = \pi$  directions, we also show in Fig. 4(a) a  $J_c$  curve for the case  $\theta = \pi/2$ . Since the rectification along the  $y$  axis is not seen, we do not show the  $\theta = 3\pi/2$  curve, as it reduces to the  $\theta = \pi/2$  case. As a way to quantify the strength of the directional asymmetry (i.e., rectification effect), we consider ratios of  $J_c(\theta, B)$  curves for different values of  $\theta$ , as shown in Fig. 4(b). It can be seen that the critical current ratios  $J_c(0, B)/J_c(\pi, B)$  and  $J_c(0, B)/J_c(\pi/2, B)$  increase with  $B$  within the considered range of magnetic field values.

Once the applied current density reaches  $J_c$ , the onset of vortex dynamics is reached. At  $J \gtrsim J_c$ , vortices remain arranged in the triangular lattice, as can be seen in the zoomed-in Cooper-pair density (CPD, quantified by  $|\Delta|^2$ ) snapshot (1) shown in Fig. 4, which is taken for  $B = 115 \text{ mT}$  and  $\theta = 0$ . Moreover, due to the sharp corners of the triangular holes, the emerging current-crowding effect can be seen, as evidenced by the increase of the supercurrent density around the triangle top vertex [33]. The increase in supercurrent density eventually facilitates the vortex depinning from the hole, where newly depinned vortices push the vortices in front of them, leading to a cascade effect resulting in some of the vortices being pushed out of the specimen. This in turn allows new vortices to enter the specimen and the cycle of vortex motion is repeated. Since vortices have a normal core, as they move the order parameter  $\Delta$  is suppressed at the front of the core and restored behind it. In this process, the Cooper pairs in front of the vortex are being converted into normal quasiparticles populating the vortex core, while the core quasiparticles relax into Cooper pairs behind the vortex. When the applied current density increases, so does the velocity of the vortex motion, resulting in the formation of regions with different vortex kinematics [34,35]. At high enough vortex velocities (i.e., applied current density), the finite conversion rate of the quasiparticles into Cooper pairs will no longer be sufficient to fully recover superconductivity behind the passing vortex before the adjacent one arrives, leading to two effects: (i) the

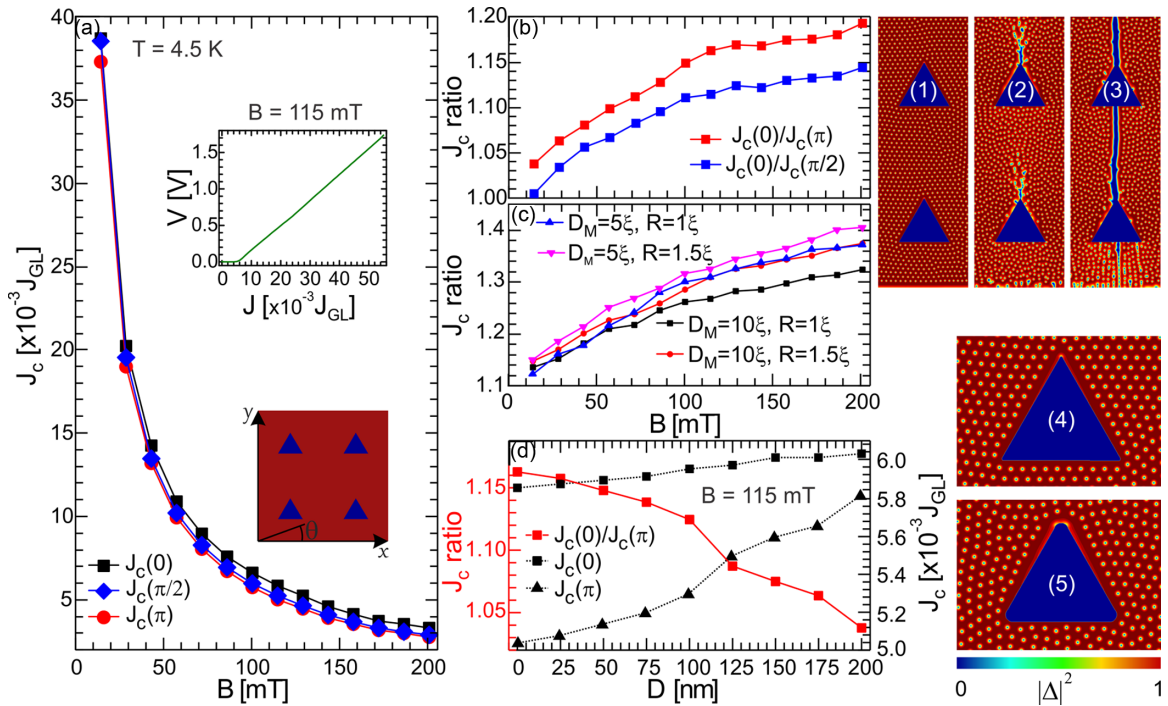


FIG. 4. (a) Critical current density  $J_c$  as a function of the applied magnetic field  $B$ , obtained for different directions of the applied current density,  $J$ , at  $T = 4.5$  K. In the adopted notation, the argument  $\theta = 0, \pi/2, \pi$  indicates the angle (measured from the positive  $x$  axis) at which  $J$  is applied.  $J_c$  values were extracted from the voltage vs current-density curves,  $V(J)$ , using a  $20 \mu\text{V}$  criterion. The upper inset in (a) shows a typical  $V(J)$  curve taken at  $115$  mT, while the lower one shows the overview of the simulated geometry. (b) Selected ratios of  $J_c(B)$  characteristics. (c) Ratio  $J_c(0, B)/J_c(\pi, B)$  as a function of  $B$  in the presence of random pinning, for the cases of median pinning distances  $D_M = 5\xi$  (dense pinning) and  $10\xi$  (sparse pinning). For each  $D_M$ , two pinning site radii  $R$  were considered, namely,  $1\xi$  and  $1.5\xi$ . (d) Ratio  $J_c(0, B)/J_c(\pi, B)$  as a function of the diameter of the hole corner,  $D$  (red full line), represented with  $J_c(0, B)$  (red squares) and  $J_c(\pi, B)$  (black squares), at  $B = 115$  mT. The Cooper-pair density snapshots (1)–(3) depict the vortex behavior: (1) at the critical current, (2) at the onset of vortex channeling from the pinning site vertices, and (3) at the onset of full vortex channeling spanning across pinning sites. The differences between the low and high curvatures of the corner diameter  $D$  are shown in insets (4) and (5), respectively, illustrating the overall impact of  $D$  on the current crowding in the system.

core of the original vortex effectively deforms from a circular to an elongated shape, and (ii) an incoming vortex experiences a region of suppressed superconductivity where there is less drag and faster motion is facilitated [36]. Finally, this results in the formation of channels of suppressed superconductivity where fast-moving flux quanta with core deformation exist. An example of the formation of such channels can be seen on the CPD snapshot (2) in Fig. 4, while snapshot (3), taken at even higher applied current density, depicts fully formed channels connecting the adjacent holes where a complete suppression of superconductivity happens. These latter events are also known as phase-slip lines.

Besides the above described main trajectory for the vortex motion (across the holes), a secondary lane of interstitial vortices moving in between the holes can also be identified. A convenient way to estimate the impact of the motion of the interstitial vortices on the overall  $J_c$  behavior is to consider a case where random pinning is present, in addition to the square lattice of holes. For this purpose, we introduced a random pinning based on a normal distribution of sites, with a geometric median distance  $D_M$  between the sites of either  $5\xi$  (dense pinning) or  $10\xi$  (sparse pinning). For each  $D_M$ , two values of pinning strength were considered, controlled by the radius of the pinning site,  $R = 1\xi$  and  $1.5\xi$ . These results are

shown in Fig. 4(c) in the form of  $J_c(0, B)/J_c(\pi, B)$  ratios as a function of the magnetic field. Similar to what we have seen in the absence of random pinning,  $J_c$  ratios follow the same profile, increasing with  $B$ , within the range of considered magnetic fields, with the sole difference of the rectification effect being slightly enhanced, as the newly added random pinning suppresses the motion of the interstitial vortices. The impact of the pinning density and strength becomes pronounced at higher fields, a region heavily cluttered by the interstitial vortices [37]. There, the sparse and low-intensity pinning yields the lowest rectification (still exceeding the no-pinning case), which then increases as the pinning intensity and density are increased.

Finally, the results presented above correspond to nearly perfect triangular holes. Real samples contain unavoidable imperfections and, in particular, rounded tips as a consequence of the limited nanofabrication resolution. In order to test the robustness of the  $J_c(0, B)/J_c(\pi, B)$  ratio, we consider several cases of holes (no random pinning) at  $T = 4.5$  K and  $B = 115$  mT with rounded corners, where a corner diameter  $D$  is varied from  $0$  to  $200$  nm, in steps of  $25$  nm. Although  $D$  estimated from scanning electron microscopy inspection does not exceed  $20$  nm, an effective rounding of the vertices could result from a border dead layer, as discussed in [38]. The

corresponding  $J_c(0, B)/J_c(\pi, B)$  ratio presented in Fig. 4(d) indicates a progressive nonlinear deterioration of the ratchet efficiency as the corners become less sharp. On the same plot, we also show that  $J_c(0, B)$  and  $J_c(\pi, B)$  increase with  $D$ . As  $D$  increases, the asymmetry imposed by very sharp hole corners becomes less influential, which in turn reduces the ratchet effect. Moreover, less sharp vertices lead to reduced current crowding, as the current density in the specimen around the holes can be more uniformly distributed. This is apparent on the zoomed-in CPD snapshots (4) corresponding to  $D = 25$  nm and (5) corresponding to  $D = 175$  nm. Indeed, for  $J = J_c$  in (4), we see a very narrow region of suppressed CPD around the vertex, from which a singular vortex can nucleate, whereas in (5), the region of suppressed CPD is much more distributed, and even two distinct vortex nucleation spots can be noticed. As a result, the reduction of the current-crowding effect with increasing  $D$  will delay the onset of vortex motion to higher currents, thus resulting in an increasing  $J_c(\theta, D)$ .

### B. Continuous electrodynamic model of the critical states

The TDGL model discussed in the previous section pointed to an anisotropic distribution of the critical current density  $J_c(\theta, B)$ , with the strongest difference arising between  $\theta = 0$  and  $\theta = \pi$ . In this section, we investigate the consequence of such an anisotropy on the critical states of the system. The model is expected to capture the physics of the problem over length scales of a few microns to a few mm, and the aim is to show that the critical current-density anisotropy arising from the triangular holes is causing the central d-line metamorphosis observed in MO images.

Returning to the symmetries of the system, the reader is reminded that for fully penetrated states, the square shape leads to a pattern of screening currents organized in four sectors with respective average flows directed along  $\theta = 0, \pi/2, \pi$ , and  $3\pi/2$ . In addition, the ratchet effect leads to different vortex dynamics between the hard and the easy directions. Thus, three different critical current densities are expected to arise. For a magnetic flux density pointing along  $+z$ , vortex motion along the easy direction ( $+y$ ) is associated with a small current density  $J_c(\pi, B)$ , whereas vortex motion along the hard direction ( $-y$ ) is associated with a large current density  $J_c(0, B) > J_c(\pi, B)$ . The current densities  $J_c(\pi/2, B)$  and  $J_c(3\pi/2, B)$ , which are, respectively, associated with vortex motion along the  $+x$  or  $-x$  directions, are expected to be equal, due to both the  $C_3$  symmetry of the triangular holes and the common  $C_4$  symmetry of the sample and the pinning array. From these symmetry considerations and the analysis carried out in Sec. IV A, we expect the inequalities  $J_c(0, B) > J_c(\pi/2, B) > J_c(\pi, B)$  to hold.

A first analysis is performed with the Bean model, assuming critical current densities that vary with the angle  $\theta$ , but do not depend on the magnetic flux density. (The argument  $B$  is therefore omitted.) Figure 5 shows the three possible patterns of d-lines (white solid lines) that may arise in a fully penetrated sample, after zero-field cooling. Current continuity across the d-lines must be satisfied in each case, yielding the following conditions:

$$J_c(0)(w - \delta w_2) = J_c\left(\frac{\pi}{2}\right)w = J_c(\pi)(w + \delta w_1), \quad (1)$$

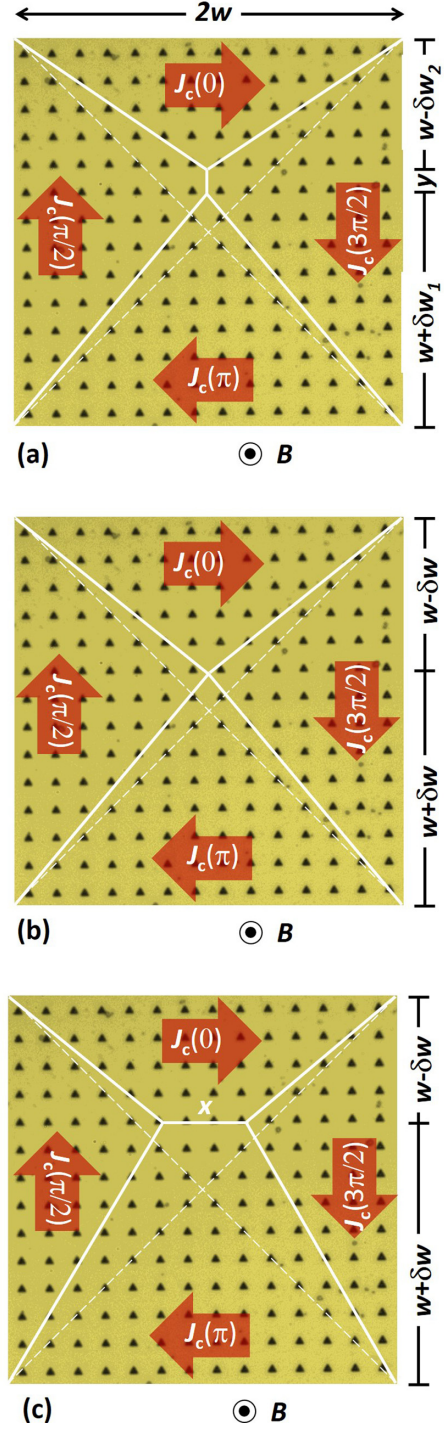


FIG. 5. Three possible patterns defined by the discontinuity lines (white solid lines) for the considered sample being magnetized after zero-field-cooling conditions, assuming  $J_c(\theta)$  independent of  $B$ . All patterns respect the inequalities  $J_c(0) > J_c(\pi/2) > J_c(\pi)$ , as long as (a)  $y = \delta w_2 - \delta w_1 > 0$  and (c)  $x < 2\delta w$ . For the sake of comparison, the pattern of d-lines corresponding to an isotropic superconductor is indicated with white dotted lines.

with  $y = \delta w_2 - \delta w_1 > 0$  for Fig. 5(a),

$$J_c(0)(w - \delta w) = J_c\left(\frac{\pi}{2}\right)w = J_c(\pi)(w + \delta w), \quad (2)$$

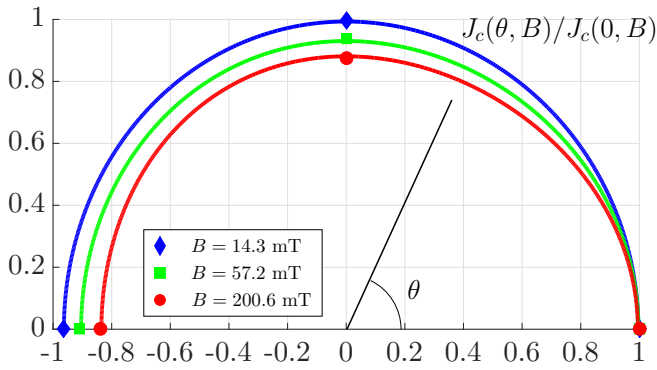


FIG. 6. Critical points  $J_c(\theta, B)/J_c(0, B)$  obtained in the TDGL approach for different intensities of the applied field. The TDGL critical points  $J_c(\theta, B)$  with  $\theta = 0, \pi/2$ , and  $\pi$  are represented for  $B_a = 14.3$  mT (diamonds), 57.2 mT (squares), and 200.6 mT (circles). The continuous curves are guides to the eye.

for Fig. 5(b), and

$$\begin{aligned} J_c(0)(w - \delta w) &= J_c\left(\frac{\pi}{2}\right)\left(w - \frac{x}{2}\right) \\ &= J_c(\pi)(w + \delta w), \end{aligned} \quad (3)$$

with  $x < 2\delta w$  for Fig. 5(c). Interestingly, these continuity conditions entail strong constraints for the following sum of ratios of critical current densities:

$$\begin{aligned} R_J &= \frac{J_c(\pi/2)}{J_c(\theta)} + \frac{J_c(\pi/2)}{J_c(\pi)} \\ &= \begin{cases} 2 - y/w < 2 & \text{for Fig. 5(a)} \\ 2 & \text{for Fig. 5(b)} \\ 2 \frac{w}{w-x/2} > 2 & \text{for Fig. 5(c),} \end{cases} \end{aligned} \quad (4)$$

so that the actual patterns realized in experiments appear to result from a delicate balance between the three current densities, and can be used as a direct probe of the intrinsic anisotropy induced by the array of holes.

It is important to note that the Bean model with a field-independent  $J_c$  [i.e.,  $J_c(\theta)$ ] is insufficient to reproduce the change in the central d-line observed in the experiments. An additional mechanism should be invoked to account for the change in  $R_J$  from values above 2 to values below 2 as the external field is decreased. The most natural extension is a magnetic field dependence, with  $J_c$  given as  $J_c(\theta, B)$ . To illustrate this dependence, we again consider the data provided by the analysis of Sec. IV A. Figure 6 shows ratios  $J_c(\theta, B)/J_c(0, B)$  obtained with the TDGL approach for three different strengths of the external field. For a fixed field, the points are consistent with a generic ovoid shape having a larger extension towards  $\theta = 0$  than  $\theta = \pi$ , with  $J_c(\pi/2, B)$  reaching an intermediate value. The continuous curves are guides to the eye to illustrate the shape of the critical surfaces. These surfaces are deformed as the external field is increased, from an almost elliptic curve for the lowest fields to ovoids exhibiting a larger difference between  $J_c(0, B)$  and  $J_c(\pi, B)$  for the largest ones.

To proceed, we use a finite-element model with a three-dimensional  $H$ - $\phi$  formulation solving Maxwell's equations in the magnetodynamic approximation (the displacement current

is neglected),

$$\dot{\mathbf{B}} = -\nabla \times \mathbf{E}, \quad \nabla \times \mathbf{H} = \mathbf{J}, \quad \text{and} \quad \nabla \cdot \mathbf{B} = 0, \quad (5)$$

where  $\mathbf{B} = \mu_0 \mathbf{H}$  and a genuine constitutive law  $\mathbf{E}(\mathbf{J})$  must be chosen, to take into account both the anisotropy and the magnetic flux density dependence of the critical current density. In the remainder of this section, we concentrate on the  $\mathbf{E}(\mathbf{J})$  law, while we present the detailed formulation used here in Appendix A 2.

The anisotropic magnetic response is introduced by means of the thermodynamic model suggested by Badia *et al.* [39,40], describing hard superconductors driven out of equilibrium with overcritical currents. In the critical state, the superconductor system is characterized by critical currents  $\mathbf{J}_c$  lying along a critical curve in the  $(J_x, J_y)$  plane. When external stimuli induce a displacement of vortices, an out-of-equilibrium state is reached with  $\mathbf{J}$  outside the critical curve. Then, the system relaxes back to equilibrium, while dissipating energy at a rate  $\mathbf{E} \cdot \mathbf{J}$ , that can be evaluated from a dissipation function  $\mathcal{F}(\mathbf{J})$ . In Ref. [39], it was shown that the transient electric field can be expressed as  $\mathbf{E} = \nabla_{\mathbf{J}} \mathcal{F}$ . This relationship serves as a thermodynamically consistent  $\mathbf{E}(\mathbf{J})$  constitutive law.

Within this theory, the main challenge in modeling the anisotropy in critical currents consists in finding an expression for  $\mathcal{F}$  that encodes the desired symmetries of the problem. It is suggested in [40] that a practically manageable function  $\mathcal{F}$  has the generic form

$$\mathcal{F} = \mathcal{F}_0(\mathcal{E}(\mathbf{J}))^M, \quad (6)$$

where  $\mathcal{E}(\mathbf{J})$  is a function of the current density with the prescribed pinning symmetries and the index  $M$  is a dimensionless parameter that depends on pinning and magnetic relaxation properties of the material. The index  $M$  is reminiscent of the critical index  $n$  appearing in the isotropic  $E = E_c (J/J_c)^n$  law. The level set  $\mathcal{F} = F_c$  defines the critical surface enclosing the critical region, which must be convex. Note that the parameter  $F_c$  can be chosen arbitrarily, similar to the fact that the critical electric field  $E_c$  in an  $E \sim J^n$  law is chosen arbitrarily.

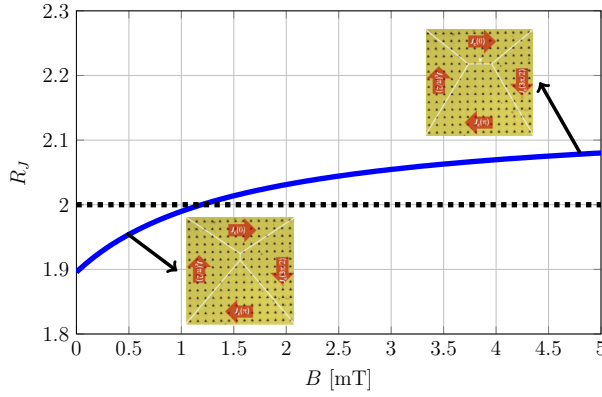
In order to identify an  $\mathbf{E}(\mathbf{J})$  law that respects the main characteristics that were revealed in the TDGL study, we seek a form of  $\mathcal{E}$  yielding a critical surface with  $J_c(0, B) > J_c(\pi/2, B) > J_c(\pi, B)$  and a continuous evolution for intermediate angles, with an ovoid shape showing an increasing ratio  $J_c(0, B)/J_c(\pi, B)$  as  $B$  is increased. To construct  $\mathcal{E}$ , we keep a minimal number of powers of  $\mathbf{J}$  and work with the ansatz

$$\mathcal{E} = \mathcal{E}_s + \mathcal{E}_a, \quad (7)$$

$$\mathcal{E}_s = \left(\frac{J_x}{J_{c,x}}\right)^2 + \left(\frac{J_y}{J_{c,y}}\right)^2, \quad (8)$$

$$\mathcal{E}_a = -\frac{C_x}{\sqrt{\mathcal{E}_s}} \left(\frac{J_x}{J_{c,x}}\right)^3, \quad (9)$$

where  $J_{c,x}$ ,  $J_{c,y}$ , and  $C_x$  are parameters that determine the ovoid extension along the main axes. Note that  $\mathcal{E}(\mathbf{J})$  is a homogeneous function of degree two. We found that this choice yields convex critical regions independent of the value of  $F_c$ .



Parameter	Value	Unit
$j_{c,x,0}$	1	MA/cm <sup>2</sup>
$B_x$	1.4	mT
$j_{c,y,0}$	0.95	MA/cm <sup>2</sup>
$B_y$	1.58	mT
$C_{x,0}$	0.15	-
$B_1$	1	mT
$B_2$	1.1	mT

FIG. 7. (a) Magnetic field dependence of the current ratio  $R_J$ . (b) Selected set of parameters.

More specifically, taking  $F_c = F_0$  yields the critical current densities

$$J_c(0, B) = \frac{J_{c,x}}{\sqrt{1 - C_x}}, \quad (10)$$

$$J_c(\pi/2, B) = J_c(3\pi/2, B) = J_{c,y}, \quad (11)$$

$$J_c(\pi, B) = \frac{J_{c,x}}{\sqrt{1 + C_x}}. \quad (12)$$

To illustrate different limits, the critical surface is a circle when  $C_x = 0$  and  $J_{c,x} = J_{c,y}$ , in which case it describes an isotropic superconductor with an  $E \sim J^n$  law where  $n = 2M - 1$ . The critical surface is an ellipse when  $C_x = 0$  and  $J_{c,x} \neq J_{c,y}$ , which corresponds to an anisotropic response without the ratchet effect. Last, in the general case with  $J_{c,x} \neq J_{c,y}$  and  $C_x > 0$ , the critical surface is not symmetric. For a proper choice of constants, it takes the form of an ovoid with  $J_c(0, B) > J_c(\pi/2, B) > J_c(\pi, B)$ , as desired.

In the system with an array of triangular holes, the shape of the ovoid is expected to vary with  $B$  and we are seeking to reproduce a situation where the critical state changes from a topology with a horizontal central d-line [Fig. 5(c)] to one with a vertical central d-line [Fig. 5(a)]. Thus, the parameters  $J_{c,x}$ ,  $J_{c,y}$ , and  $C_x$  are allowed to vary with  $B$  in such a way that the current ratio  $R_J$  in Eq. (4) decreases from a value larger than 2 at large  $B$  to one below 2 at small  $B$ . The parameters  $J_{c,x}$  and  $J_{c,y}$  are assumed to follow Kim's law [41]. For  $C_x$ , we choose a bounded, continuous, and strictly increasing function of  $B$ . Thus, we have

$$J_{c,x} = \frac{j_{c,x,0}}{1 + B/B_x}, \quad (13)$$

$$J_{c,y} = \frac{j_{c,y,0}}{1 + B/B_y}, \quad (14)$$

$$C_x = C_{x,0} \frac{B + B_1}{B + B_2}, \quad (15)$$

with seven parameters  $j_{c,x,0}$ ,  $B_x$ ,  $j_{c,y,0}$ ,  $B_y$ ,  $C_{x,0}$ ,  $B_1$ , and  $B_2$  to be appropriately chosen.

We seek parameters that respect the constraints that were revealed by the TDGL analysis:  $J_c(0, B) > J_c(\pi/2, B) > J_c(\pi, B)$  for all  $B$ , with an anisotropy  $J_c(0, B)/J_c(\pi, B)$  that increases with  $B$  [see Fig. 4(b)]. Further,  $R_J(B)$  is required to be an increasing function of  $B$ , which equals 2 and yields

the d-line structure of Fig. 5(b) for  $B \sim 1$  mT, as indicated by the experiments in Fig. 2. The set of parameters in Fig. 7(b) satisfies all these requirements and produces a succession of critical states that follows the experimental observations, as illustrated in Fig. 8 for a selection of critical states obtained while decreasing the applied field after an initial magnetization to 5 mT. One can see that the central critical line is horizontal for external fields higher than 1 mT, degenerates into a single point at  $\mu_0 H_a \sim 1$  mT, and then becomes vertical as  $H_a$  is further lowered to reach the remanent state. The

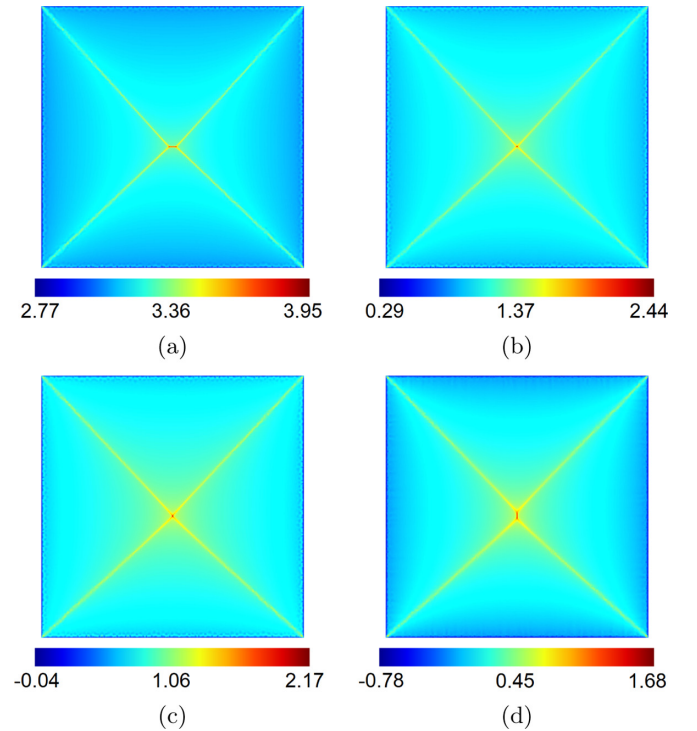


FIG. 8. Out-of-plane component of the simulated magnetic flux density,  $\mu_0 H_z$ , for different applied fields  $H_a$ . The magnetic flux density is expressed in mT. The set of parameters used is that in Fig. 7(b). The critical states shown correspond to the decreasing stage after having applied a maximum flux density of 5 mT, with either (a)  $\mu_0 H_a = 3.11$  mT, (b)  $\mu_0 H_a = 1$  mT, (c)  $\mu_0 H_a = 0.75$  mT, or (d) the remanent state.



corresponding curve of  $R_J$  as a function of  $B$  is shown in Fig. 7(a).

A few comments are in order. First, a parametrization based on the TDGL numerical results can be found that yields a similar succession of critical states, however, with a d-line metamorphosis taking place at fields that are larger than  $\sim 1$  mT. This should not come as a surprise, as even though the studied TDGL system has a density of holes similar to the experimental sample, it only contains a few holes and is thus different from the sample. Here, the TDGL study is used to reveal the main characteristics in the current anisotropy and the retained parametrization is chosen to reproduce the experimental orders of magnitude. Second, it appears that while a transformation of the central d-line is easy to obtain by implementing a magnetic field dependence, a metamorphosis from a horizontal to a vertical line requires one to identify the proper parameters. In practice, we found that under moderate variations of the parameters, one may obtain a succession of critical states in the wrong order—a vertical line transforming into a horizontal one. This behavior suggests that while the d-line pattern can reveal fairly small asymmetries in the system (the current anisotropy is of the order of a few percent), the critical states result from a delicate balance between the different current densities. A third comment concerns the model main assumption, i.e., that the anisotropy in the current densities is homogeneous. More specifically, the  $C_4$  symmetry of the hole network is ignored, together with the likely occurrence of channels of propagation of the magnetic flux along its principle axes. The current formalism with convex  $\mathcal{F}$  functions would need to be adapted to include this additional symmetry. A last comment concerns the adequacy of our findings with the experimental pictures in Fig. 2. The model proposed here provides a plausible mechanism for explaining the transformation of the central d-line, namely, that the ratchet effect, embodied in the  $\theta$  dependence of the critical surface  $J_c(\theta, B)$ , needs to be field dependent. While our model reproduces the d-line structures of the observed critical states, it can be seen that other experimental characteristics are not captured. The simulated central lines are shorter than the experimental ones. Moreover, the simulated central d-line respects a left-right mirror symmetry, whereas the experimental line appears to be shifted to the left and to the bottom as  $H_a$  is decreased. The two lower experimental oblique lines also seem to have “kinks” for certain values of  $H_a$ . These discrepancies might be due to the presence of defects that perturb the magnetic flux penetration and possibly introduce asymmetries that are not included in our model.

### C. Numerical modeling of thermomagnetic flux instabilities

Several ingredients ruling the magnetic flux penetration were not accounted for by the phenomenological model presented in the previous section. First, the actual array of triangular holes was indirectly considered by an effective pinning yielding an anisotropic current density, while the detailed geometry of the pinning array was ignored. Second, the possible local thermal heating caused by rapid flux motion was neglected. In this section, we numerically investigate the influence of these two effects on the morphology of the flux penetration.

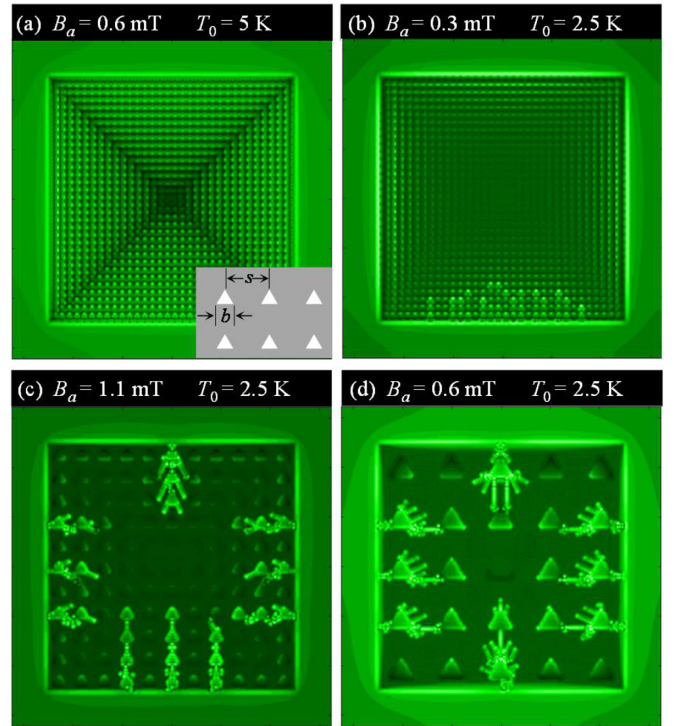


FIG. 9. Magnetic flux distribution in a superconducting film with a periodic pinning array of equilateral triangular holes of side  $b$  and period  $s$ , obtained by numerical simulations for (a)  $T_0 = 5$  K,  $B_a = 0.6$  mT,  $J_{c0s}/d = 1.2 \times 10^{11}$  A/m<sup>2</sup>,  $b = 76.5$   $\mu$ m,  $s = 127.6$   $\mu$ m; (b)  $T_0 = 2.5$  K,  $B_a = 0.3$  mT,  $J_{c0s}/d = 1.2 \times 10^{11}$  A/m<sup>2</sup>,  $b = 76.5$   $\mu$ m,  $s = 127.6$   $\mu$ m; (c)  $T_0 = 2.5$  K,  $B_a = 1.1$  mT,  $J_{c0s}/d = 3.6 \times 10^{11}$  A/m<sup>2</sup>,  $b = 178.6$   $\mu$ m,  $s = 408.2$   $\mu$ m; and (d)  $T_0 = 2.5$  K,  $B_a = 0.6$  mT,  $J_{c0s}/d = 1.2 \times 10^{11}$  A/m<sup>2</sup>,  $b = 382.7$   $\mu$ m,  $s = 994.9$   $\mu$ m.

In the numerical simulations, we consider a square superconducting film with size of  $2w = 5$  mm and thickness of  $d = 45$  nm, which is exposed to a gradually increasing transverse magnetic field. The superconducting film is assumed to be in thermal contact with a substrate which is kept at a constant temperature  $T_0$  (i.e., the environmental temperature). The superconducting film contains a periodic array of equilateral triangular holes of side  $b$  and period  $s$  [see inset in Fig. 9(a)].

The electrodynamics of the superconducting film exposed to a transverse magnetic field is obtained by solving Maxwell’s equations in the magnetodynamic approximation (the displacement current is neglected),

$$\dot{\mathbf{B}} = -\nabla \times \mathbf{E}, \quad \nabla \times \mathbf{H} = \mathbf{J}_s \delta(z), \quad \text{and} \quad \nabla \cdot \mathbf{B} = 0, \quad (16)$$

with  $\mathbf{B} = \mu_0 \mathbf{H}$  and  $\nabla \cdot \mathbf{J}_s = 0$ . Here, the film thickness  $d$  is neglected against the other characteristic length scales and thus the current density is given as  $\mathbf{J}_s \delta(z)$ , with  $\mathbf{J}_s$  the sheet current and  $\delta(z)$  the Dirac delta distribution.

The time evolution of the temperature in the system is governed by the heat propagation equation

$$dc\dot{T} = d\kappa \nabla^2 T - h(T - T_0) + \mathbf{J}_s \cdot \mathbf{E}, \quad (17)$$

where  $\kappa$  and  $c$  are the thermal conductivity and the specific heat of the superconducting film,  $h$  is the coefficient of heat transfer between the superconducting film and the substrate,

and  $T_0$  is the substrate temperature which is kept constant. The thermal parameters  $\kappa$ ,  $c$ , and  $h$  are assumed to be proportional to  $T^3$  [42].

The constitutive relationship between current and electric field is given by [42]

$$\mathbf{E} = \rho(J_s)\mathbf{J}_s/\mathbf{d}, \quad (18)$$

with a nonlinear resistivity,

$$\rho(J_s) = \begin{cases} \rho_0(J_s/J_{cs})^{n-1}, & J_s \leq J_{cs}, T \leq T_c \\ \rho_0, & J_s > J_{cs}, T \leq T_c \\ \rho_n, & T > T_c, \end{cases} \quad (19)$$

where  $\rho_0$  is a constant,  $\rho_n$  is the normal state resistivity,  $J_{cs}$  is the critical sheet current density, and  $n$  is the flux creep exponent. The temperature dependencies are taken as

$$J_{cs} = J_{c0s}(1 - T/T_c) \quad \text{and} \quad n = n_0T_c/T, \quad (20)$$

where  $J_{c0s}$  and  $n_0$  are constants. Equations (16) together with the material law are numerically solved by an efficient Fourier real-space hybrid algorithm and the integral method (see details in Refs. [42,43]) with boundary conditions setting  $\rho = \rho_n$  in the holes (see Ref. [44]). Simulations details and parameters are given in Appendix A 3.

Figures 9(a) and 9(b) show the contour plots of the magnetic field distribution in a superconducting film with a periodic array of small triangular holes for common parameters and different working temperatures  $T_0$ . Since exactly reproducing the  $1.5 \times 10^6$  triangular holes of the experimental sample requires prohibitively large computing resources, we limit the simulations to an array of  $N \times N$  holes with  $N = 32$ . For the high temperature of 5 K, the flux smoothly penetrates to the center of the film without any thermomagnetic instability and eventually a clear X-shape d-line is formed [Fig. 9(a)], which is consistent with the experimental result at  $\mu_0H = 1.37$  mT, which is shown in Fig. 2. This indicates that the magnetic field morphology induced by current flow is not sensitive to the asymmetry of triangle holes. For the low temperature ( $T_0 = 2.5$  K), however, several fingerlike flux avalanches are observed at  $B_a = 0.3$  mT [Fig. 9(b)]. Note that the flux avalanches first nucleate at the bottom edge and then develop along the easy direction, as revealed by the experiment (see Fig. 3).

As the size of the holes could affect the crowding level of current flow around the holes, we further investigate the flux avalanches in the superconducting films with a periodic array of triangular holes of different sizes. For intermediate triangular holes ( $b = 178.6 \mu\text{m}$ ,  $s = 408.2 \mu\text{m}$ ), the first avalanche is also triggered at the bottom edge and subsequently other magnetic flux avalanches appear along the other borders [Fig. 9(c)]. Moreover, it can be seen that the morphology of avalanches entering from the bottom is fingerlike, whereas those originating from other sides exhibit sideways branching. The branches of dendritic flux avalanches from the upper edge are likely to develop and grow along the two corners of the triangular holes, which can be clearly observed in the superconducting film with even bigger holes [see Fig. 9(d)]. One can see that a narrow channel consisting of magnetic flux moving from the sample borders to the closest triangular holes is first formed. When the flux channel with elevated

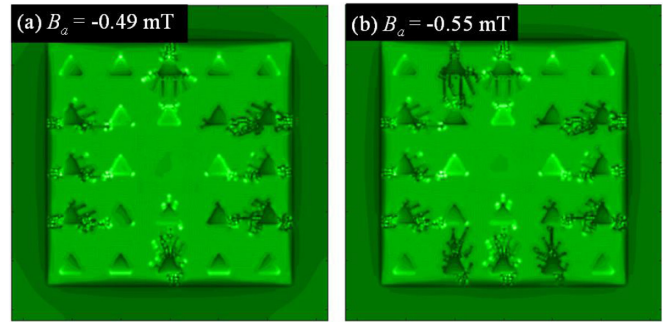


FIG. 10. Magnetic flux distribution of superconducting films with a periodic array of equilateral triangular holes of side  $b = 382.7 \mu\text{m}$  and period  $s = 994.9 \mu\text{m}$ , in a decreasing magnetic field with  $\dot{B}_a = -5$  T/s after the applied field increase to 6 mT at  $T_0 = 2.5$  K.

temperature [45] reaches the holes, the magnetic flux fills the triangular holes through these channels. Then, the secondary avalanches are triggered at the sharp corners of the triangular holes, which spread to neighboring holes. To conclude, the avalanches occurring at the bottom edge and developing along the vertical upward direction are more likely to form fingerlike morphology, while the flux avalanches triggered at the upper edge will spread laterally along the bottom corners of the triangular holes to form more branched avalanches. Since the size of the triangular holes affects the morphology and size of the flux avalanches, considering that all the triangular holes in our simulations are much larger than those in the experimental samples, the morphology of the avalanches shown in Fig. 9 cannot perfectly replicate the experimental results. Notwithstanding the hole size difference, the simulated anisotropy of flux avalanches is consistent with the results observed in experiments.

In Fig. 10, we show the flux avalanches in the superconducting film shown in Fig. 9(d), which is exposed to a decreasing applied magnetic field after it was first increased to 0.6 mT. Bright regions correspond to positive penetrated flux; dark areas represent negative flux (antiflux). As shown in Fig. 10(a), there are several reversed flux avalanches occurring in the film, all of them nucleating near the avalanches already triggered during the increasing field and penetrating the film through the same tracks, which is consistent with the experimental results reported in Ref. [46]. By comparing Fig. 10(a) with Fig. 9(d), one can find that the antiflux penetrates the film and is trapped by the hole, so that the flux in the holes is gradually restored. When the applied magnetic field is further reduced to  $-0.55$  mT, as shown in Fig. 10(b), three antiflux avalanches are triggered and expand along new paths. Notice that a larger negative flux is trapped by the holes in this process. Overall, the avalanches of antiflux triggered in a decreasing field prefer to reuse the paths of the flux avalanches which were created by the increasing field.

## V. CONCLUSIONS

We considered samples with a noncentrosymmetric pinning texture induced by a square array of triangular holes.

We investigated the resulting magnetic flux rectification effect for both the smooth flux penetration and the thermomagnetic instability regimes. For the former regime, the magneto-optical images revealed a pattern of discontinuity lines that evolves under decreasing fields, with the central horizontal line metamorphosing into a vertical one. A time-dependent Ginzburg-Landau model showed that the array of holes leads to a ratchet effect, with critical current densities distributed as a function of the angle along a critical line in the form of an ovoid. The TDGL analysis further revealed that vortices nucleate at the vertices of the triangular holes and then preferentially move from hole to hole, whereas interstitial vortices see their motion hampered by bulk pinning. This scenario is robust for small variations of pinning strengths, defect sizes, and also a moderate rounding of the triangular hole vertices. An analysis of the magnetic flux distribution at the level of continuous electrodynamics showed that the observed evolution of the central d-line can be reproduced, provided that two essential properties are satisfied: (i) the system shows a ratchet effect with an asymmetry for currents flowing parallel to the bases of the triangular holes, and (ii) the critical current densities vary with the local magnetic flux density.

For the thermomagnetically unstable regime, experiments showed anisotropic bursts of magnetic flux, with vortices preferentially leaving the triangular holes from their vertices, in accordance with the precursor behavior observed in the TDGL calculations. Further calculations at the continuous electrodynamics level showed that avalanches developing along the easy direction have a fingerlike morphology, whereas those occurring in the opposite direction spread laterally and yield additional branches, as vortices leave the holes through lateral vertices. When the field is reduced after an initial magnetization, the antflux avalanches tend to reuse the path of avalanches triggered during the field increase, thereby confirming the earlier experimental results of Ref. [46].

These findings show that noncentrosymmetric pinning textures can induce rectification of the magnetic flux penetration, bring subtle modifications to the critical state profiles, and affect the morphology of magnetic flux avalanches. While an anisotropic pinning can be exploited to guide the flux penetration in magnetic flux lenses, observing the evolution of the critical states with the external field can be used as a macroscopic tool to determine their efficiency.

#### ACKNOWLEDGMENTS

This work is supported in part by the Fonds de la Recherche Scientifique - FNRS, under Grants No. U.N027.18 and No. T.0204.21, the COST actions CA16218 and CA19108, and Research Foundation - Flanders (FWO). L.J. and C.X. acknowledge the support by the National Natural Science Foundation of China (Grants No. 11972298 and No. 11702218). The authors also acknowledge the Brazilian agencies São Paulo Research Foundation (FAPESP, Grants No. 2007/08072-0 and No. 09/10818-5), Coordenação de Aperfeiçoamento de Pessoal de Nível Superior - Brasil (CAPES)-Finance Code 001, and National Council of Scientific and Technologic Development (CNPq).

M.M. and L.B. contributed equally to this work.

#### APPENDIX: NUMERICAL MODELS AND METHODS

##### 1. TDGL method

The TDGL framework provides the information about the spatiotemporal distribution of the inhomogeneous superconducting complex order parameter,  $\Delta(\mathbf{r}, t)$ , in the presence of the magnetic vector potential  $\mathbf{A}(\mathbf{r}, t)$  and the electrostatic potential  $\varphi(\mathbf{r}, t)$ . The underlying dimensionless equations of the model are

$$u \frac{\partial \Delta}{\partial t} = (\nabla - i\mathbf{A})^2 \Delta + (1 - |\Delta|^2) \Delta - i\varphi \Delta \quad (\text{A1})$$

and

$$\nabla^2 \varphi = \nabla(|\Delta|^2 [\nabla \Theta - \mathbf{A}]), \quad (\text{A2})$$

where time is given in units of  $\tau_{GL}(T) = \pi \hbar / 8k_B T_c u f(T)$  ( $\hbar$  is the reduced Planck's constant,  $k_B$  is the Boltzmann constant,  $u = 5.79$  is the average ratio of the relaxation times of the order parameter amplitude  $|\Delta(\mathbf{r}, t)|$  and the order parameter phase  $\Theta(\mathbf{r}, t)$  [47], and  $f(T) = 1 - T/T_c$  is the thermal kernel carrying the temperature dependence of the system), corresponding to the Ginzburg-Landau (GL) relaxation time. All distances are expressed in units of the coherence length,  $\xi(T) = \xi(0)/\sqrt{f(T)}$ . The order parameter is scaled with its bulk value,  $\Delta_{GL}(T) = 4\sqrt{uk_B T_c}/\pi\sqrt{f(T)}$ , while the units of electrostatic and magnetic potentials are  $\varphi_{GL}(T) = \hbar/e^* \tau_{GL}(T)$  and  $A_{GL}(T) = B_{c2}(T)\xi(T)$ , respectively [ $e^* = 2e$  is the charge of the Cooper pair and  $B_{c2}(T) = \Phi_0/2\pi\xi^2(T)$  is the bulk upper critical magnetic field, also used to scale the overall magnetic field  $B$ , with  $\Phi_0$  being the magnetic flux quantum]. The unit of the current density  $J$  is  $J_{GL}(T) = \sigma_n \varphi_{GL}(T)/\xi(T)$ , where  $\sigma_n$  is the electrical conductivity of the system.

The applied electrical current density  $J_a$  is injected into the system via the boundary conditions describing the superconductor-normal (SN) interface  $\nabla\varphi(\mathbf{r}_{NS}) = \mathbf{J}_a$  (i.e., the normal contacts, where  $\mathbf{r}_{NS}$  denotes the SN interface region) along which the condition  $\Delta(\mathbf{r}_{NS}) = 0$  must also be satisfied. Along the direction perpendicular to the flow of the current density, superconductor-vacuum (SV) boundaries are applied, preventing leakage of both the supercurrent density  $(\nabla - i\mathbf{A})\Delta(\mathbf{r}_{SV}) = 0$  ( $\mathbf{r}_{SV}$  denotes the SV interface region) and the normal current density  $\nabla\varphi(\mathbf{r}_{SV}) = 0$  through these boundaries. During the investigation of  $J_c(\theta, B)$  behavior, in the cases  $\theta = 0$  and  $\theta = \pi$ , the SN region was located between  $y = 0$  and  $y = L$ , along the entire  $x$  direction (where the sign of the applied current was reversed between the cases  $\theta = 0$  and  $\pi$ ). For  $\theta = \pi/2$ , the SN region was located between  $x = 0$  and  $x = L$ , along the entire  $y$  direction. The voltage  $V$  was extracted as an average of the electrostatic potential difference  $\Delta\varphi = \varphi(\mathbf{r}_1) - \varphi(\mathbf{r}_2)$ , where regions  $\mathbf{r}_1$  and  $\mathbf{r}_2$  are lines parallel to the normal contacts and separated from them each by a distance of  $40\xi$ . Simulations of the dynamics of the superconducting condensate are performed on a computational grid of size  $\Delta x = \Delta y = 0.1 \times \xi(T)$ , where, for each value of applied current density and magnetic field, the duration of the simulation was set to  $10^5 \times \tau_{GL}(T)$  time units in order to guarantee that either the steady state or the state of

the dynamic equilibrium is reached. The bath temperature of the system was set to 4.5 K.

## 2. Continuous electrodynamics approach with a finite-element formulation

We use a finite-element model with a three-dimensional  $H$ - $\phi$  formulation. The simulation domain  $\Omega$  contains the superconducting film, defining a conducting domain  $\Omega_c$ , embedded in a nonconducting domain  $\Omega_c^c = \Omega/\Omega_c$ . The domain  $\Omega$  is discretized in elements and the magnetic field  $\mathbf{H}$  is approximated as a linear combination of elementary functions as follows:

$$\mathbf{H} = \mathbf{H}_a + \mathbf{h}, \quad (\text{A3})$$

$$\mathbf{h} = \sum_{e_i \in \Omega_c} a_i \boldsymbol{\psi}_i + \sum_{n_j \in \Omega_c^c} b_j \nabla \phi_j, \quad (\text{A4})$$

where  $\mathbf{H}_a$  and  $\mathbf{h}$  are the applied and the reaction fields, respectively. The functions  $\boldsymbol{\psi}_i$  are linear and defined on the element edges  $e_i$  of  $\Omega_c$  (excluding its surface), while  $\phi_j$  are linear nodal functions defined on the nodes of  $\Omega_c^c$  (including the surface of  $\Omega_c$ ). The coefficients  $a_i$  and  $b_j$  are the unknowns of the problem. The  $H$ - $\phi$  formulation follows from a standard integration of Faraday's law over  $\Omega$ , leading to a weak formulation of the problem [48]. Additionally, we follow the method introduced in [49] to avoid truncation errors which are inherent to the finite extension of the simulating domain. Shell transformations [50] are implemented

over a region  $\Omega/\Omega_b$ , where  $\Omega_b$  is an arbitrary region which includes  $\Omega_c$ .

The simulation domain is meshed with GMSH [51], while the  $H$ - $\phi$  formulation is solved with GETDP [52]. The simulated domain consists in a series of 13 extruded layers of the same planar unstructured mesh (Delaunay triangulation). The mesh size varies from 10  $\mu\text{m}$  in the central area of the film, where the metamorphosis of the d-line is observed, to 50  $\mu\text{m}$  along the film borders and 5 mm along the boundary of the transformation shell. The discretization in time is made with finite differences using an implicit Euler method. At each time step, the nonlinear equations are resolved with Newton-Raphson iterations until the residual is lower than an absolute value of  $10^{-6}$  or the relative difference between the current and the first iterative step is lower than  $10^{-6}$ . The time stepping is adapted according to the required number of iterations.

## 3. Continuous electrodynamics simulations of avalanches

The simulations are implemented on a domain with a rectangular area of  $2L_x \times 2L_y$  discretized on  $256 \times 256$  equidistant grids, where  $L_x = L_y = 1.3w$  and  $w$  is the half size of the square sample in the simulations. The superconducting parameters used in the numerical simulations are given as  $T_c = 6.8$  K,  $J_{c0s}/d = 1.2 \times 10^{11}$  A/m<sup>2</sup>, and  $\rho_0 = \rho_n = 5 \times 10^{-9}$   $\Omega\text{m}$  [29]. The thermal parameters vary with temperature as  $\kappa = 20$  W/Km  $\times (T/T_c)^3$ ,  $h = 10^4$  W/Km<sup>2</sup>  $\times (T/T_c)^3$ , and  $c = 3 \times 10^4$  W/Km<sup>3</sup>  $\times (T/T_c)^3$ , respectively [29]. We adopt  $n_0 = 20$  and limit the creep exponent to  $n(T) \leq 100$  for convergence issues [45]. The superconducting film is exposed to an increasing magnetic field ramped at a rate  $\dot{B}_a$ , from an initial zero-field-cooled state.

- 
- [1] R. P. Feynman, R. B. Leighton, and M. Sands, *The Feynman Lectures on Physics* (Addison-Wesley, Reading, 1963), Vol. 1, Chap. 46.
- [2] J. M. R. Parrondo and P. Español, *Am. J. Phys.* **64**, 1125 (1996).
- [3] M. O. Magnasco, *Phys. Rev. Lett.* **71**, 1477 (1993).
- [4] P. Hänggi and F. Marchesoni, *Rev. Mod. Phys.* **81**, 387 (2009).
- [5] S. Matthias and F. Müller, *Nature (London)* **424**, 53 (2003).
- [6] G. Mahmud, C. J. Campbell, K. J. M. Bishop, Y. A. Komarova, O. Chaga, S. Soth, S. Huda, K. Kandere-Grzybowska, and B. A. Grzybowski, *Nat. Phys.* **5**, 606 (2009).
- [7] X. Jiang, D. A. Bruzewicz, A. P. Wong, M. Piel, and G. M. Whitesides, *Proc. Natl. Acad. Sci.* **102**, 975 (2005).
- [8] P. Galajda, J. Keymer, P. Chaikin, and R. Austin, *J. Bacteriol.* **189**, 8704 (2007).
- [9] M. B. Wan, C. J. Olson Reichhardt, Z. Nussinov, and C. Reichhardt, *Phys. Rev. Lett.* **101**, 018102 (2008).
- [10] P. K. Ghosh, V. R. Misko, F. Marchesoni, and F. Nori, *Phys. Rev. Lett.* **110**, 268301 (2013).
- [11] A. Guidobaldi, Y. Jeyaram, I. Berdakin, V. V. Moshchalkov, C. A. Condat, V. I. Marconi, L. Giojalas, and A. V. Silhanek, *Phys. Rev. E* **89**, 032720 (2014).
- [12] H. Linke, B. J. Alemán, L. D. Melling, M. J. Taormina, M. J. Francis, C. C. Dow-Hygelund, V. Narayanan, R. P. Taylor, and A. Stout, *Phys. Rev. Lett.* **96**, 154502 (2006).
- [13] G. Lagubeau, M. Le Merrer, C. Clanet, and D. Quéré, *Nat. Phys.* **7**, 395 (2011).
- [14] C.-S. Lee, B. Jankó, I. Derényi, and A.-L. Barabasi, *Nature (London)* **400**, 337 (1999).
- [15] J. F. Wambaugh, C. Reichhardt, C. J. Olson, F. Marchesoni, and F. Nori, *Phys. Rev. Lett.* **83**, 5106 (1999).
- [16] J. E. Villegas, S. Savel'ev, F. Nori, E. M. Gonzalez, J. V. Anguita, R. Garcia, and J. L. Vicent, *Science* **302**, 1188 (2003).
- [17] V. Rouco, A. Palau, C. Monton, N. Del-Valle, C. Navau, A. Sanchez, X. Obradors, and T. Puig, *New J. Phys.* **17**, 073022 (2015).
- [18] J. Albrecht, A. T. Matveev, J. Stremper, H. U. Habermeier, D. V. Shantsev, Y. M. Galperin, and T. H. Johansen, *Phys. Rev. Lett.* **98**, 117001 (2007).
- [19] M. Menghini, J. Van de Vondel, D. G. Gheorghe, R. J. Wijngaarden, and V. V. Moshchalkov, *Phys. Rev. B* **76**, 184515 (2007).
- [20] D. V. Denisov, A. L. Rakhmanov, D. V. Shantsev, Y. M. Galperin, and T. H. Johansen, *Phys. Rev. B* **73**, 014512 (2006).
- [21] P. de Gennes, *Superconductivity of Metals and Alloys* (Westview, Boulder, CO, 1999).
- [22] D. Cerbu, V. N. Gladilin, J. Cuppens, J. Fritzsche, J. Tempere, J. T. Devreese, V. V. Moshchalkov, A. V. Silhanek, and J. Van de Vondel, *New J. Phys.* **15**, 063022 (2013).

- [23] C. Jooss, J. Albrecht, H. Kuhn, S. Leonhardt, and H. Kronmüller, *Rep. Prog. Phys.* **65**, 651 (2002).
- [24] L. E. Helseth, R. W. Hansen, E. I. Ilyashenko, M. Baziljevich, and T. H. Johansen, *Phys. Rev. B* **64**, 174406 (2001).
- [25] M. Pannetier, R. J. Wijngaarden, I. Fløan, J. Rector, B. Dam, R. Griessen, P. Lahl, and R. Wördenweber, *Phys. Rev. B* **67**, 212501 (2003).
- [26] A. V. Silhanek, L. Van Look, S. Raedts, R. Jonckheere, and V. V. Moshchalkov, *Phys. Rev. B* **68**, 214504 (2003).
- [27] M. S. Welling, R. J. Wijngaarden, C. M. Aegerter, R. Wördenweber, and P. Lahl, *Physica C* **404**, 410 (2004).
- [28] D. G. Gheorghe, M. Menghini, R. J. Wijngaarden, S. Raedts, A. V. Silhanek, and V. V. Moshchalkov, *Physica C* **437-438**, 69 (2006).
- [29] M. Motta *et al.*, *Phys. Rev. B* **89**, 134508 (2014).
- [30] F. Colauto, M. Motta, and W. Ortiz, *Supercond. Sci. Technol.* **34**, 013022 (2021).
- [31] O.-A. Adami, Ž. L. Jelić, C. Xue, M. Abdel-Hafiez, B. Hackens, V. V. Moshchalkov, M. V. Milošević, J. Van de Vondel, and A. V. Silhanek, *Phys. Rev. B* **92**, 134506 (2015).
- [32] J. Van de Vondel, V. N. Gladilin, A. V. Silhanek, W. Gillijns, J. Tempere, J. T. Devreese, and V. V. Moshchalkov, *Phys. Rev. Lett.* **106**, 137003 (2011).
- [33] J. R. Clem and K. K. Berggren, *Phys. Rev. B* **84**, 174510 (2011).
- [34] A. V. Silhanek, M. V. Milošević, R. B. G. Kramer, G. R. Berdiyrov, J. Van de Vondel, R. F. Luccas, T. Puig, F. M. Peeters, and V. V. Moshchalkov, *Phys. Rev. Lett.* **104**, 017001 (2010).
- [35] L. Embon, Y. Anahory, Ž. L. Jelić, E. O. Lachman, Y. Myasoedov, M. E. Huber, G. P. Mikitik, A. V. Silhanek, M. V. Milošević, A. Gurevich, and E. Zeldov, *Nat. Commun.* **8**, 85 (2017).
- [36] D. Y. Vodolazov and F. M. Peeters, *Phys. Rev. B* **76**, 014521 (2007).
- [37] W. V. Pogosov, V. R. Misko, H. J. Zhao, and F. M. Peeters, *Phys. Rev. B* **79**, 014504 (2009).
- [38] I. Charaev, T. Silbernagel, B. Bachowsky, A. Kuzmin, S. Doerner, K. Ilin, A. Semenov, D. Roditchev, D. Yu. Vodolazov, and M. Siegel, *Phys. Rev. B* **96**, 184517 (2017).
- [39] A. Badía-Majós and C. López, *Supercond. Sci. Technol.* **25**, 104004 (2012).
- [40] A. Badía-Majós and C. López, *Supercond. Sci. Technol.* **28**, 024003 (2015).
- [41] Y. B. Kim, C. F. Hempstead, and A. R. Strnad, *Phys. Rev. Lett.* **9**, 306 (1962).
- [42] J. I. Vestgarden, D. V. Shantsev, Y. M. Galperin, and T. H. Johansen, *Phys. Rev. B* **84**, 054537 (2011).
- [43] E. H. Brandt, *Phys. Rev. B* **52**, 15442 (1995).
- [44] L. Prigozhin and V. Sokolovsky, *Supercond. Sci. Technol.* **31**, 055018 (2018).
- [45] J. I. Vestgarden, F. Colauto, A. M. H. de Andrade, A. A. M. Oliveira, W. A. Ortiz, and T. H. Johansen, *Phys. Rev. B* **92**, 144510 (2015).
- [46] M. Motta, F. Colauto, R. Zadorosny, T. H. Johansen, R. B. Dinner, M. G. Blamire, G. W. Ataklti, V. V. Moshchalkov, A. V. Silhanek, and W. A. Ortiz, *Phys. Rev. B* **84**, 214529 (2011).
- [47] R. J. Watts-Tobin, Y. Krähenbühl, and L. Kramer, *J. Low Temp. Phys.* **42**, 459 (1981).
- [48] A. Bossavit, *IEEE Proc. A* **135**, 493 (1988).
- [49] L. Burger, C. Geuzaine, F. Henrotte, and B. Vanderheyden, *COMPEL* **38**, 1441 (2019).
- [50] F. Henrotte, B. Meys, H. Hedia, P. Dular, and W. Legros, *IEEE Trans. Magn.* **35**, 3 (1999).
- [51] C. Geuzaine and J.-F. Remacle, *Int. J. Numer. Methods Eng.* **79**, 1309 (2009).
- [52] P. Dular, C. Geuzaine, F. Henrotte, and W. Legros, *IEEE Trans. Magn.* **34**, 3395 (1998).